Delft University of Technology

Sub-Nappe Air Cavity Pressure During Overflow of a Vertical Structure

Kim, Taeksang; Malherbe, Julien; Shimpalee, Sirawit; Bricker, Jeremy

Citation (APA)
Kim, T., Malherbe, J., Shimpalee, S., & Bricker, J. (2023). Sub-Nappe Air Cavity Pressure During Overflow of a Vertical Structure. In D. Cox (Ed.), *Proceedings of the 37th International Conference on Coastal Engineering, ICCE 2022* (37 ed.). (Proceedings of the Coastal Engineering Conference; No. 37). American Society of Civil Engineers (ASCE).

Important note
To cite this publication, please use the final published version (if applicable).
Please check the document version above.

SUB-NAPPE AIR CAVITY PRESSURE DURING OVERFLOW OF A VERTICAL STRUCTURE

Taeksang Kim[1] and Julien Malherbe[2] and Sirawit Shimpalee[3] and Jeremy Bricker[4][5]

Megathrust earthquakes cause tsunamis that can destroy coastal structures and damage buildings, resulting in injuries and deaths. To prevent these consequences and reduce the risk of failure of coastal structures, it is essential to understand the exact mechanism of structure failure. Sub-nappe air cavity pressure during overflow of a vertical structure, which is the main topic of this research, can increase the risk of failure of structure, but had not yet been quantified. In this research, hydraulic experiments were conducted to reveal the relation among the air cavity pressure, overtopping flowrate, and tailwater depth for aerated and non-aerated overflow cases. For the aerated case, we found that air cavity pressure is almost equal to the atmospheric pressure regardless of flowrate and downstream weir height. On the other hand, for the non-aerated case or a partially-aerated case, air cavity pressure is inversely proportional to overtopping flowrate. The relation between air cavity pressure and tailwater depth could be interpreted in different ways based on the flow condition downstream.

Keywords: sub-nappe air cavity pressure; vertical structure; hydraulic experiment

Introduction

Vertical structures such as seawalls and caisson breakwaters are fundamental to the construction of ports and harbors. They protect coastal infrastructure from natural disasters such as storms or tsunamis, but also could be destroyed by such disasters. The 2004 Sumatra tsunami (Suppasri et al., 2012), Hurricane Katrina in 2005 (Seed et al., 2008), the 2011 Tohoku (Japan) tsunami (Bricker et al., 2012), and Typhoon Haiyan in 2013 (Bricker et al., 2014) contain examples of such structures destroyed.

The types of failures experienced by vertical structures are various. Sliding or overturning due to hydrostatic / hydrodynamic forces are one of the failure types, but insufficient bearing capacity of the foundation could also contribute to failure of structures (Takahashi, 2002). For instance, during the 2011 Great East Japan tsunami, the sliding force and bearing capacity of the foundation were key factors to the widespread damage of caissons (Takagi and Bricker, 2015). This tsunami killed 15,889 lives in Fukushima, Miyagi, Iwate, and other prefectures, and more than 2,600 people are still missing (National Police Agency of Japan, 2014). In the case of Tohoku, caisson breakwaters were destroyed due to a combination of sliding (Takagi, 2015), foundation bearing capacity failure (punching; Bricker et al., 2013), and foundation scour (Arikawa et al., 2012; Jayaratne et al., 2014). Additionally, floodwalls of both gravity (T-wall, L-wall) and cantilever (I-wall) types were destroyed due to overflow-induced scour (Chock et al., 2013) followed by overturning.

Among different failure modes of vertical structures, sliding and overturning failures are considered as the most dominant failure modes of vertical structures. Sliding failure occurs when the horizontal external force acting on structure is greater than the static friction force of the structure, and overturning failure occurs when the overturning moments acting on structure are larger than the resisting moments.

Over the years, progress has been made to prevent sliding and overturning failure. Friction mats between caisson and rubble mound foundation have been proposed to reduce the probability of sliding failure (Suppasri et al., 2016). Arikawa et al. (2012), based on laboratory and numerical experiments, suggested that the water level difference between the windward and leeward side is one of the major causes of the sliding failure of the vertical structure during tsunami overflow. However, despite this progress in the design of vertical structures, there is still much that is unknown, which needs to be addressed to prevent sliding and overturning failure.

Sub-nappe air cavity pressure during overflow of a vertical caisson, which is our main topic in the research, is a subject which needs to be quantified. Vertical structures are vulnerable to sliding and overturning failure when exposed to water levels high enough to cause overflow. In other words, the stability of vertical structures such as caisson breakwater can be deteriorated by the overflow jet. Based on Chanson (1996) who is a pioneer of air-water flow, air bubble entrainment takes place along the cavity interface (also called nappe aeration) and at the end of the cavity by re-entrant jet mechanism. See Fig.1.

---

[1] Civil and Environmental Engineering, University of Michigan, 2350 Hayward St, Ann Arbor, MI, 48109, USA
[2] Civil and Environmental Engineering, University of Michigan, 2350 Hayward St, Ann Arbor, MI, 48109, USA
[3] Civil and Environmental Engineering, University of Michigan, 2350 Hayward St, Ann Arbor, MI, 48109, USA
[4] Civil and Environmental Engineering, University of Michigan, 2350 Hayward St, Ann Arbor, MI, 48109, USA
[5] Hydraulic Engineering, Delft University of Technology, 2628 CN, Delft, the Netherlands

When air is entrained from the air cavity below the nappe into the overflowing water, the pressure in the cavity becomes lower than that of the atmosphere. This sub-atmospheric pressure on the leeward wall of the caisson generated by non-aerated overflow causes an additional horizontal force, and it eventually increases the sliding force and the probability of sliding or bearing capacity failure.
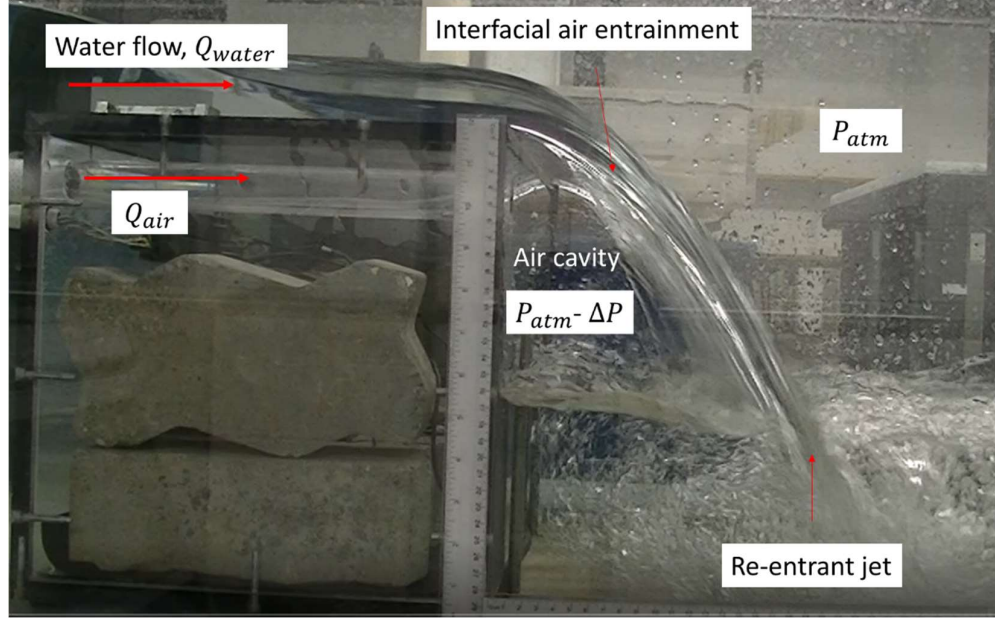

Figure 1. Air entrainment mechanisms in the ventilated cavity flow

In order to understand the relation between the sub-atmospheric cavity pressure and overflow jet properties, an analytical model, experimental studies, and Computational Fluid Dynamics (CFD) model studies were proposed. Mudiyanselage (2017) calculated sub-atmospheric pressure in the cavity and the additional horizontal force acting on the model by using experimental methods and CFD modeling, but this research has a limitation in that the majority of numerical simulations are modeled as 2D simulations. Patil et al. (2018) based on laboratory and numerical experiments using 3D simulations, hinted that the sliding force increased up to 20% due to non-aerated overflow, so this constant percentage of force increase is currently suggested by the ASCE7-22 Chapter 6 guideline for tsunami overflow of vertical structures. However, the actual relation among sub-atmospheric pressure in the cavity, tsunami wave form, and caisson geometry is still unknown. This research aims to reveal this relation through laboratory experiments.

Methodology

Flume and caisson model

A HM 161 Experimental flume manufactured by GUNT Hamburg is installed in the hydraulic laboratory at the University of Michigan. Fig. 2 represents the front view of the HM 161 flume. It has an experimental section with transparent side walls of $16\ [m]$ which allows observation of experiments and a cross-section of $0.6\ [m] \times 0.8\ [m]$. The bottom wall is constructed with stainless-steel and the side walls are constructed with plexiglass. The outlet of the flume contains a plate weir with an adjustable height. We constructed a cuboid shaped vertical caisson model at the University of Michigan. It is $0.3\ [m]$ long (in the streamwise direction) and has a cross-section of $0.6\ [m] \times 0.3\ [m]$. Similar to the flume, the model was made with plexiglass so that the inside of the model can be observed. The top wall of the model is fixed by screws, so it can be removed when needed.

Fig. 3 represents the rear view of the vertical caisson model box. Two water pressure sensors are fixed on the inside of the model. Although the sensor probes measure voltage signal in water, the interior part of the sensors should be kept in the dry environment of the box as they are not waterproof. Six holes on the downstream side wall of the model were constructed to connect sensor probes from the inside of the box. The elevation of the six holes are $0.025, 0.075, 0.125, 0.175, 0.225, 0.275\ [m]$ respectively

from the bottom of the flume. Two sensor probes are connected into two of the holes for each experiment and the unused holes are sealed with O-ring screws.
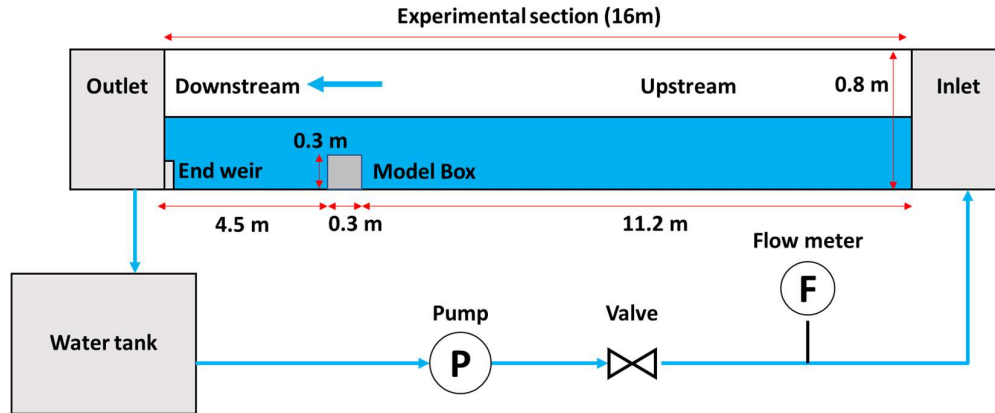

Figure 2. A schematic of the closed water circuit for the HM 161 flume

Heavy weight materials such as bricks and lead lie on the inside of the model to prevent sliding and overturning due to hydrostatic force. Two steel rods were installed in front of the downstream side wall of the box for the same purpose. Since our research assumes two-dimensional flow, foam pieces were wedged in the gap between the flume side wall and the model to prevent transversal water flow.

Our research considers an aerated condition and a non-aerated condition. The aerated condition was created by connecting a snorkel of PVC tubing from the air cavity, through the model, and up to the surface, while the non-aerated condition was created by closing this tubing. An air pressure sensor measures the pressure in the cavity.
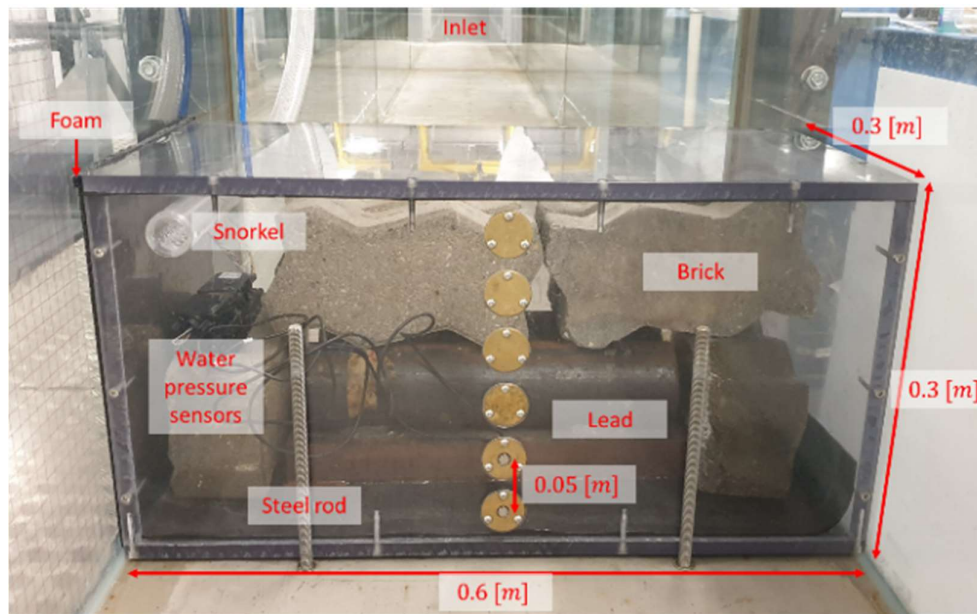

Figure 3. Rear view of the vertical caisson model box

Pressure sensors and DAQ system

Two Kulite Miniature high-pressure transducers (HKM-375 series) were used as the water pressure sensors and a KSC-2 signal conditioner was used to maximize the measurement capability of the sensors as shown in Fig. 4. 15 [m] wire extensions were used to connect the pressure sensors in the caisson model to the signal condition. The pressure range of water pressure sensors is 1 [bar] and the specified accuracy

of these sensors is $\pm0.1\%$ of full scale (FS) range. Therefore, the error of these sensors does not exceed 100[Pa] or -100[Pa] at any point in the pressure range ($\because$ 1[bar] $\times \pm0.1\% = \pm100$[Pa]).

A "Dwyer Series 616KD Differential Pressure Transmitter" was used as an air pressure sensor. Fig. 5 shows the basic setup for the air pressure sensor. Since this sensor is not waterproof, we connected the sensor to the snorkel with small PVC tubing threaded through the large aerated PVC tubing. In this way, we can measure the air pressure at the end of the snorkel. The pressure range of the air pressure sensor is 3 [$inch\ of\ water\ column$] = 746.52 [Pa] and the specified accuracy of this sensor is $\pm2\%$ of full scale range, which means the error of this air pressure sensor does not exceed 15[Pa] or -15[Pa] at any point in the pressure range ($\because$ 746.52[Pa] $\times \pm2\% \approx 15$[Pa]).
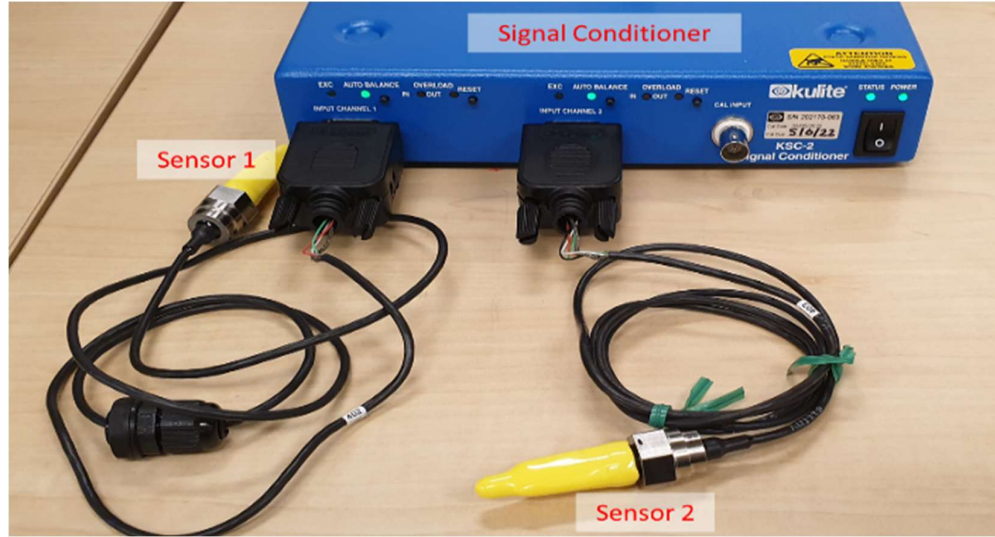

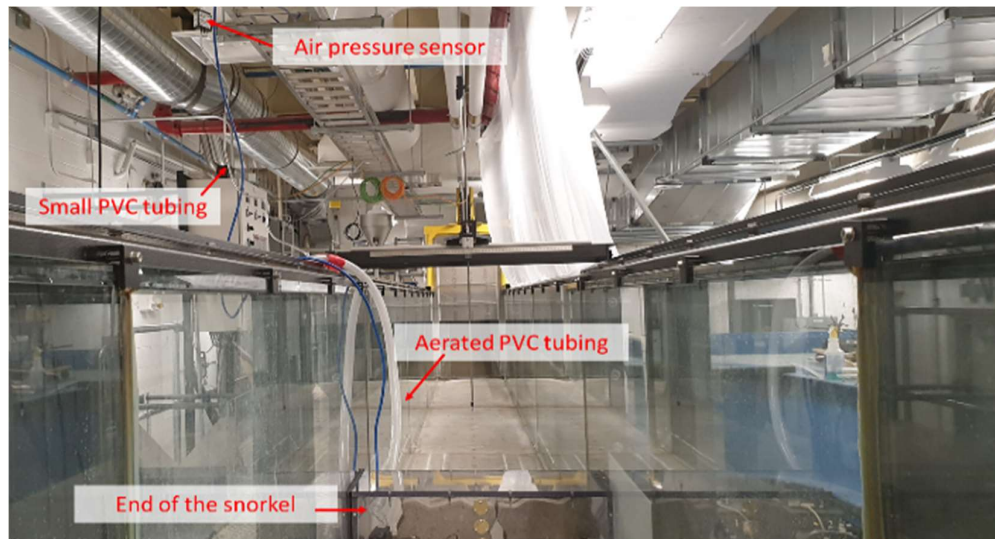**Figure 4. Water pressure sensors and it's signal conditioner**

Figure 5. Setup for air pressure sensor

A National Instruments (NI) Data Acquisition System (DAQ System) is used to acquire the electric signal from the different sensors. Fig. 6 represents the basic setup of hardware of DAQ Systems in this research. A NI cDAQ 9174 chassis was used for the basic frame of DAQ Systems and a total of four NI 9207 modules in Fig. 6 can be mounted on this frame. NI 9207 module has 16 channels, which are composed of 8 voltage signal channels and 8 current signal channels. Each of two water pressure sensors used one voltage signal channel. On the other hand, the air pressure sensor used one current signal

channel. In order to connect these sensors into each channel, a NI 9923 connector was used in our research as shown in Fig. 6. In order to provide optimal data quality, we used chassis ground condition through the amplifier (KSC-2) input power cord to earth ground via the third wire earth ground at the wall outlet and this provides a low-noise, low-impedance, earth ground reference to internal amplifier circuitry. DAQExpress by NI was used for the data acquisition software. We can acquire and analyze the data obtained from sensors using DAQExpress. Water and air pressure data were acquired for 5 min durations for each experiment and the sampling rate of both sensors was 83 Hz. The two water pressure sensors measured voltage in the range -10 [V] to 10 [V] and the air pressure sensor measured current in the range 3.85 [mA] to 20 [mA]. Measured voltage and current datum were converted to pressure data through a hydrostatic (water-filled tube) calibration process.
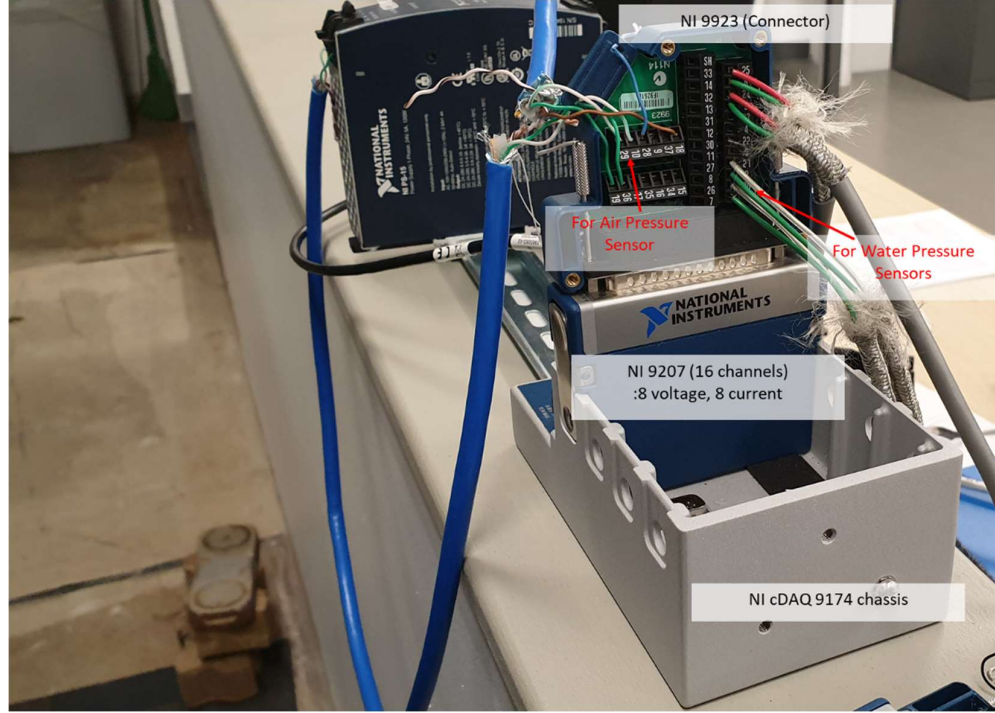

Figure 6. Hardware of DAQ systems

Results

Determination of flow condition downstream of the model

   While the flow condition upstream of the instrumented box in our experiment is always subcritical flow, the flow condition downstream of the box could be different based on the value of the flowrate. It is important to check the flow condition downstream because the relation among variables in our experiment could be different according to the flow condition downstream. For instance, if the flow condition downstream is supercritical, the weir height at end of the flume could not affect the cavity pressure because water level downstream of the box would be always lower than critical depth y_c (in this case a hydraulic jump exists between the flow downstream of the box and the weir at the end of the flume). The flow behavior in an open channel depends on the Froude number. The Froude number is defined as the ratio of the inertia force to the gravitational force. For a rectangular cross-section with uniform water depth h, the Froude number can be expressed as Eq. 1.

$$\text{Fr} = \frac{U}{\sqrt{gh}} = \frac{Q}{A\sqrt{gh}} = \frac{Q}{bh\sqrt{gh}} = \frac{Q}{b\sqrt{gh^3}} \quad (1)$$

Where

$Q = $ Discharge $\left[\frac{m^3}{hr}\right]$, $b = $ Width of the channel $[m]$

$h = $ Water depth $[m]$, $g = $ Gravitational acceleration

When the gravitational force is the dominant force in the flow, this flow is regarded as subcritical flow and the Froude number is lower than 1.0. On the other hand, when the inertia force is the dominant, this flow is regarded as supercritical flow and the Froude number is higher than or equal to 1.0. Thus, we can calculate the critical depth of each experimental case by manipulating Eq. 1 into Eq. 2. Table 1 contains the calculated critical depth y_c based on the different upstream flowrates which were used in our experiment when a width of the channel b was set to 0.6 [m].

$$1 = \frac{Q}{b\sqrt{gh^3}} \quad \rightarrow \quad h = y_c = \left(\frac{Q^2}{gb^2}\right)^{1/3} \quad (2)$$

Where

y_c = Critial depth $[m]$, Q = Discharge $\left[m^3/hr\right]$
b = Width of the channel $[m]$, g = Gravitational acceleration

Table 1. Critical depth of flow according to the flowrates		
Surcharge above the box $(y-\eta)$ $[m]$	$Q\left[m^3/hr\right]$	y_c $[m]$
0.055	52	0.039
0.061	61	0.043
0.065	67	0.046
0.083	97	0.059
0.101	131	0.072

Table 1 also contains the surcharge above the box $y-\eta$ and it was used to validate the upstream water flowrate Q. Fig. 7 represents the relation between the surcharge above the box and the upstream water flowrate and it can be expressed like Eq. (3) from the regression method. Theoretically, the upstream water flowrate is proportional to surcharge above the box to the power of 1.5 based on Francis weir equation and the obtained relation is consistent with Francis weir equation.

$$Q = 4245.7(y-\eta)^{1.5177} \quad (3)$$

Where

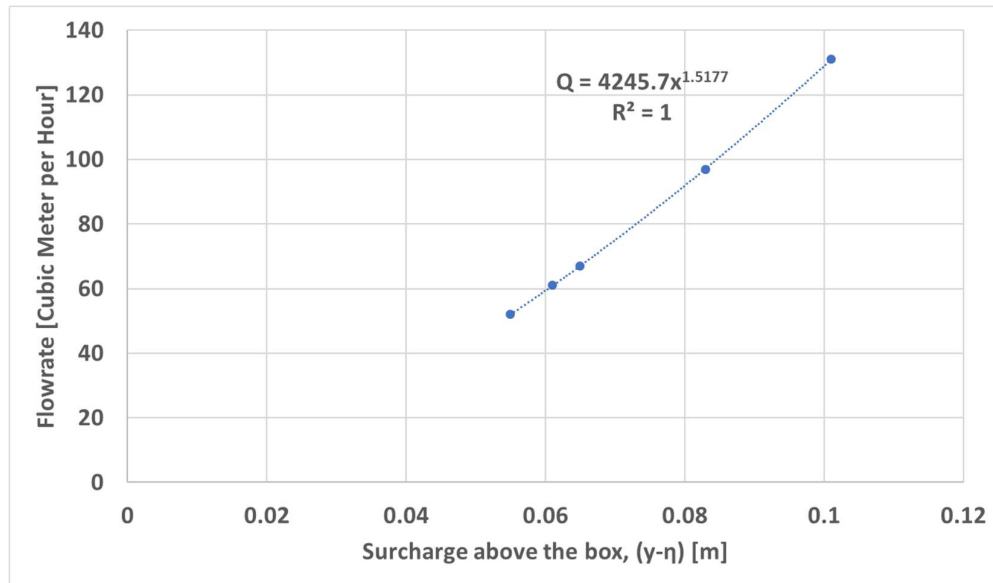Q = Discharge $\left[m^3/hr\right]$, $y-\eta$ = Surcharge above the box $[m]$

Figure 7. Upstream water flowrate as a function of surcharge above the box

The flow condition downstream of the box could be determined by comparing the water depth downstream, y_d in Fig. 8 measured by digital level gauge with the critical depth, y_c in Table 1. When the water depth downstream is greater than the critical depth, the flow condition downstream is subcritical, and when the water depth downstream is less than the critical depth, the flow condition downstream is supercritical. Table 2 shows the flow condition downstream of the box for different flowrates and end weir heights, h_{weir}.

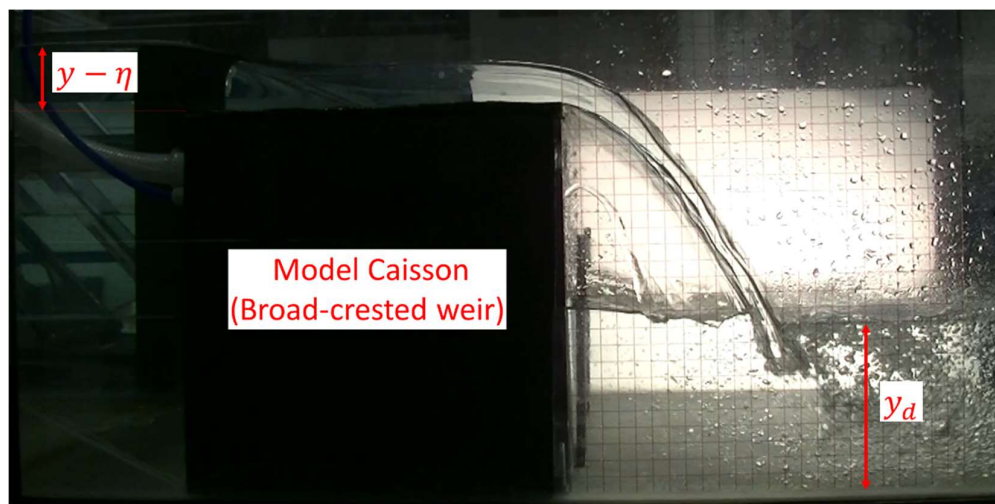| Table 2. Flow condition downstream of the box for different flowrates and downstream weir heights				
$Q\left[\frac{m^3}{hr}\right]$	$y_c\,[m]$	$h_{weir} = 0.1[m]$	$h_{weir} = 0.125[m]$	$h_{weir} = 0.15[m]$
52	0.039	Sub-crit.	Sub-crit.	Sub-crit.
61	0.043	Sub-crit.	Sub-crit.	Sub-crit.
67	0.046	Sub-crit.	Sub-crit.	Sub-crit.
97	0.059	Super-crit.	Super-crit.	Sub-crit.
131	0.072	Super-crit.	Super-crit.	Sub-crit.

Figure 8a. Subcritical flow downstream when the downstream water depth is greater than the critical depth

Figure 8b. Supercritical flow downstream when the downstream water depth is less than the critical depth

Relation of cavity pressure to water flowrate and end weir height

Five different water flowrates, Q of (52, 61, 67, 97, 131) $\left[\frac{m^3}{hr}\right]$ and three different end weir heights, h_{weir} of 0.1 [m], 0.125 [m], 0.15 [m] were used in this research for both the aerated and the non-aerated cases. Each experiment lasted 5 minutes, and was repeated five times for a total of 150 experiments 5 (flowrates) × 3 (weir heights) × 2 (aeration conditions) × 5 (repetitions). Mean water levels and air pressure values were extracted from each steady-state time series.

    1.   Cavity pressure as a function of water flowrate

Fig. 9 shows the relation between the gauge pressure in the air cavity and the water flowrate, for a model caisson height of 0.3 [m] and downstream weir heights of 0.1 [m], 0.125 [m], 0.15 [m]. The air cavity pressure of the non-aerated case was lower than that of the aerated case, which is consistent with Patil et al. (2018). For the non-aerated case, water flowrate and air cavity pressure are observed to have a negative linear correlation, with R-squared values similar to that shown in Fig. 9. On the other hand, for the aerated case, air cavity pressure is near zero for low water flowrates (52, 61, 67) $\left[\frac{m^3}{hr}\right]$, but decreases below zero for high water flowrates (97, 131) $\left[\frac{m^3}{hr}\right]$, similar to the non-aerated case. Theoretically, the air cavity pressure of the aerated case should be almost zero if enough artificial aeration was supplied to the cavity. However, the diameter of the PVC tubing was not large enough, so the aerated case became only partially aerated for high water flowrates, which lead to negative air pressure values.
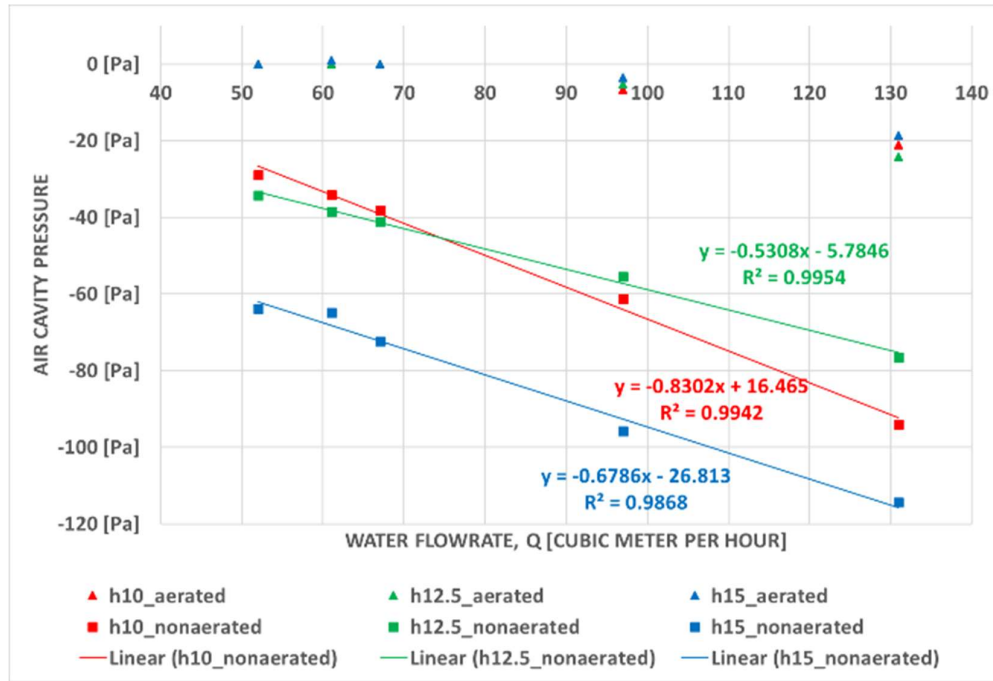

Figure 9. Air cavity pressure as a function of water flowrate

    2.   Cavity pressure as a function of end weir height

Fig. 10 shows the relation between the air cavity pressure and the weir height, for a model caisson height of 0.3 [m] and water flowrates of (52, 61, 67, 97, 131) $\left[\frac{m^3}{hr}\right]$. For the aerated case, the air cavity pressure values are approximately zero for low water flowrates of (52, 61, 67) $\left[\frac{m^3}{hr}\right]$, regardless of weir height. When the water flowrate is high (yellow and black dashed lines), the air cavity pressure is negative but approximately constant for all weir heights. On the other hand, for the non-aerated case, two different patterns are shown in Fig. 10. When the water flowrate is low (red, green, and blue solid lines in Fig. 10), the air cavity pressure decreases as the weir height increases. When the water flowrate is high

(yellow and black solid lines in Fig. 10), the air cavity pressure values increase initially from weir heights of 0.1 [m] to 0.125 [m], and then decrease from weir heights of 0.125 [m] to 0.15 [m]. It is difficult to interpret these different patterns, but one possibility is to consider the two different flow patterns: 1) Subcritical flow and 2) Supercritical flow. Upstream flow is always subcritical flow in this research, but downstream flow could vary based on water flowrate and downstream weir height. When the water flowrate increases and the weir height decreases, the downstream flow tends to become supercritical flow. For low water flowrates (red, green, and blue solid lines in Fig. 10), upstream and downstream flows were all subcritical flow, regardless of the weir height. In that case, the air cavity pressure decreases as the weir height increases. On the other hand, for high water flowrates (yellow and black solid lines in Fig. 10), the downstream flow was supercritical flow for weir heights of 0.1 [m] and 0.125 [m], and the air cavity pressure increases as the weir height increases in that case. However, the downstream flow becomes subcritical for a weir height of 0.15 [m], and the air cavity pressure decreases from 0.125 [m] to 0.15 [m].
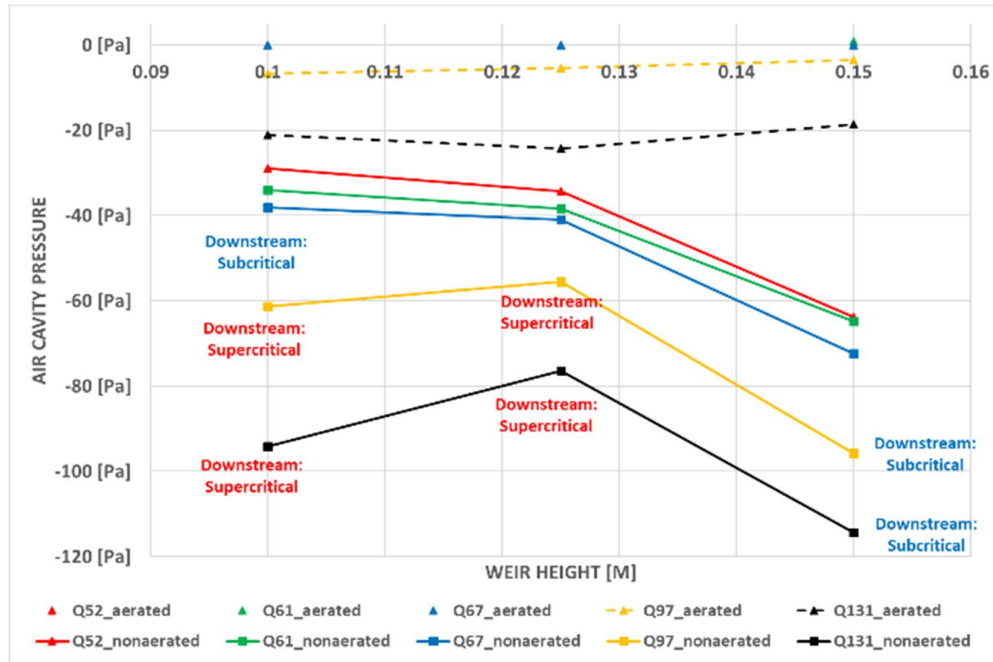

Figure 10. Air cavity pressure as a function of end weir height

3.   Water pressure as a function of water flowrate

Fig. 11 represents the relation between the water pressure measured at 0.025 [m] from the bottom and the water flowrate, for a model caisson height of 0.3 [m] and weir heights of 0.1 [m], 0.125 [m], 0.15 [m]. Fig. 11 shows three different patterns. First, the water pressure of the non-aerated case is larger than that of the aerated case. This result can be verified by comparing the solid line and the dashed line in Fig. 11. This result makes sense because the free-surface below the cavity increases in height due to lower cavity air pressure in the non-aerated case. Second, the water pressure value increases as the weir height increases, which can be checked by comparing the different colored lines. This result also makes sense because water column height below the jet corresponds to a larger depth of water above the pressure sensor, which leads to higher water pressures. Lastly, there is no significant relation between the water flowrate and the water pressure. In result (B), we concluded that the water flowrate affects the air cavity pressure significantly. However, as shown in Fig. 11, there is no apparent relationship between water flowrate and water pressure, with the water pressure increasing or decreasing inconsistently for different water flowrates. Therefore, water flowrate does not seem to be an important parameter affecting water pressure, while weir height is likely a key factor affecting water pressure.
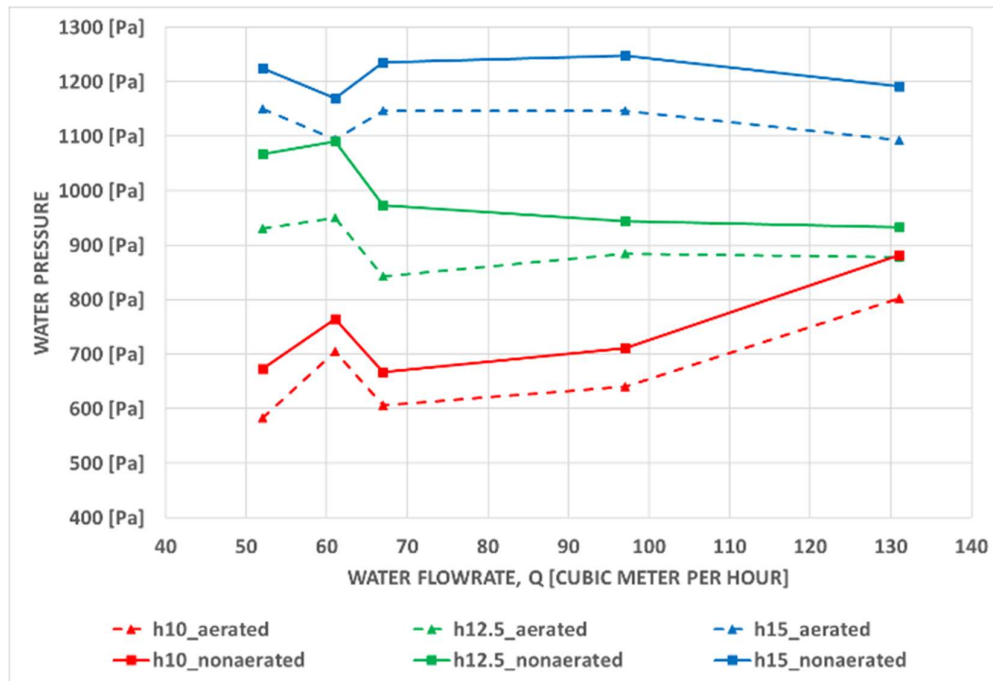
Figure 11. Water pressure as a function of water flowrate

Conclusion

In this research, hydraulic experiments were conducted in order to reveal how air cavity pressure is affected by water flowrate and end weir height for aerated and non-aerated overflow conditions. Before starting the main experiments, we performed pressure sensor calibration and water flowrate calibration to ensure accurate results. Through the main experiments, we found three results. First, we observe that water flowrate and air cavity pressure have a negative linear correlation for the non-aerated condition and the partially aerated conditions. Second, the relation between air cavity pressure and end weir height could be interpreted in two different ways based on the downstream flow condition. If the downstream flow is subcritical, the air cavity pressure becomes more negative as the downstream weir height increases. On the other hand, if downstream flow is supercritical, the air cavity pressure becomes less negative as the downstream weir height increases. Last, we observe that water flowrate is not an important parameter affecting water pressure acting on the model caisson, while weir height is likely a key factor affecting water pressure. In summary, we found the relation among air cavity pressure, water flow rate, and end weir height for aerated and non-aerated cases. This research could be used as a basis to explain how overflow of a structure can increase the probability of failure of the structure.

REFERENCES

Arikawa, T., Sato, M., Shimosako, K., Hasegawa, I., Yeom, G.S. and Tomita, T., 2012. Failure mechanism of Kamaishi breakwaters due to the Great East Japan earthquake tsunami. *Coastal engineering proceedings*, *1*(33), p.16.

Bricker, J.D., Francis, M. and Nakayama, A., 2012. Scour depths near coastal structures due to the 2011 Tohoku Tsunami. *Journal of hydraulic research*, *50*(6), pp.637-641.

Bricker, J.D., Takagi, H. and Mitsui, J., 2013. Turbulence model effects on VOF analysis of breakwater overtopping during the 2011 Great East Japan Tsunami. In *Proceedings of the 2013 IAHR World Congress* (Vol. 10153).

BRICKER, J.D., TAKAGI, H., MAS, E., KURE, S., ADRIANO, B., YI, C. and ROEBER, V., 2014. Spatial variation of damage due to storm surge and waves during Typhoon Haiyan in the Philippines. *土木学会論文集 B2 (海岸工学)*, *70*(2), pp.I_231-I_235.

Chanson, H., 1996. *Air bubble entrainment in free-surface turbulent shear flows*. Elsevier.

Chock, G., Robertson, I., Kriebel, D., Francis, M. and Nistor, I., 2013, June. Tohoku, Japan, earthquake and tsunami of 2011: Performance of structures under tsunami loads. American Society of Civil Engineers.

Jayaratne, R., Abimola, A., Mikami, T., Matsuba, S., Esteban, M. and Shibayama, T., 2014. Predictive model for scour depth of coastal structure failures due to tsunamis. *Coastal Engineering Proceedings*, (34), pp.56-56.

Patil, A., Mudiyanselage, S.D., Bricker, J.D., Uijttewaal, W. and Keetels, G., 2018. Effect of overflow nappe non-aeration on tsunami breakwater failure. *Coastal Engineering Proceedings*, (36), pp.18-18.

Seed, R.B., Bea, R.G., Athanasopoulos-Zekkos, A., Boutwell, G.P., Bray, J.D., Cheung, C., Cobos-Roa, D., Ehrensing, L., Harder Jr, L.F., Pestana, J.M. and Riemer, M.F., 2008. New Orleans and Hurricane Katrina. II: the central region and the lower Ninth Ward. *Journal of geotechnical and geoenvironmental engineering*, *134*(5), pp.718-739.

Suppasri, A., Koshimura, S., Imai, K., Mas, E., Gokon, H., Muhari, A. and Imamura, F., 2012. Damage characteristic and field survey of the 2011 Great East Japan Tsunami in Miyagi Prefecture. *Coastal Engineering Journal*, *54*(1), pp.1250005-1.

Suppasri, A., Latcharote, P., Bricker, J.D., Leelawat, N., Hayashi, A., Yamashita, K., Makinoshima, F., Roeber, V. and Imamura, F., 2016. Improvement of tsunami countermeasures based on lessons from The 2011 Great East Japan Earthquake and Tsunami—situation after five years. *Coastal Engineering Journal*, *58*(4), pp.1640011-1.

Takagi, H., 2015. Method for quick assessment of caisson breakwater failure due to Tsunamis: Retrospective analysis of data from the 2011 Great East Japan Earthquake and Tsunami. *Coastal Engineering Journal*, *57*(3), pp.1550012-1.

Takagi, H. and Bricker, J.D., 2015. Breakwater damage and the effect of breakwaters on mitigation of inundation extent during tsunamis: Case study of the 2011 Great East Japan earthquake and tsunami. In *Handbook of coastal disaster mitigation for engineers and planners* (pp. 363-383). Butterworth-Heinemann.

Takahashi, S., 2002. Design of vertical breakwaters. *PHRI reference document nr. 34*.